ACS APPLIED MATERIALS & INTERFACES

Research Article

www.acsami.org

# Analog Memristors Based on Thickening/Thinning of Ag Nanofilaments in Amorphous Manganite Thin Films

Dongqing Liu,[†] Haifeng Cheng,*[,†] Xuan Zhu,[‡] Guang Wang,[§] and Nannan Wang[†]

[†]Science and Technology on Advanced Ceramic Fibers and Composites Laboratory, National University of Defense Technology, Changsha 410073, P. R. China

[‡]State Key Laboratory of High Performance Computing, National University of Defense Technology, Changsha 410073, P. R. China

[§]College of Science, National University of Defense Technology, Changsha 410073, P. R. China

Supporting Information

**ABSTRACT:** We developed an analog memristor based on the thickening/thinning of Ag nanofilaments in amorphous $La_{1-x}Sr_xMnO_3$ (a-LSMO) thin films. The Ag/a-LSMO/Pt memristor exhibited excellent pinched hysteresis loops under high-excitation frequency, and the areas enclosed by the pinched hysteresis loops shrank with increasing excitation frequency, which is a characteristic typical of a memristor. The memristor also showed continuously tunable synapselike resistance and stable endurance. The a-LSMO thin films in the memristor acted as a solid electrolyte for $Ag^+$ cations, and only the Ag/a-LSMO/Pt memristor electroformed with a larger current compliance easily exhibited high-frequency pinched hysteresis loops. On the basis of the electrochemical metallization (ECM) theory and electrical transport models of quantum wires and nanowires, we concluded that the memristance is ultimately determined by the amount of charge supplied by the external current. The state equations of the memristor were established, and charge was the state variable. This study provides a new analog memristor based on metal nanofilaments thickening/thinning in ECM cells, which can be extended to other resistive switching materials. The new memristor may enable the development of beyond von Neumann computers.

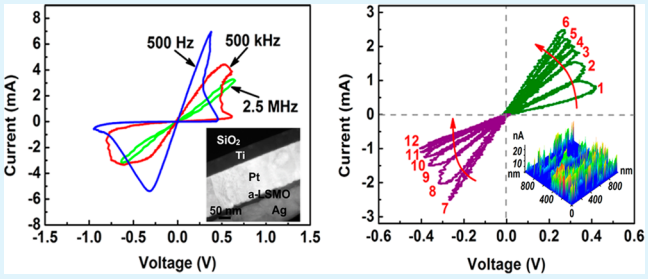


**KEYWORDS:** *analog memristor, amorphous Manganite thin film, nanofilament, pinched hysteresis loop, resistive switching, conductance quantization*

## INTRODUCTION

Memristors are two-terminal nonlinear dynamic resistors that retain an internal resistance state depending on the past history of input current or voltage. Leon Chua[1] first theoretically predicted the existence of memristors in 1971 as the fourth basic circuit element in addition to the three classical elements: resistors, capacitors, and inductors. Although the experiments leading to the development of memristors go back 2 centuries,[2] Strukov et al.[3] did not develop the first physical $TiO_2$-based memristor until 2008. Although the memristor was originally defined as components that linked charge and flux, they were more often described as devices that showed a frequency-dependent pinched hysteresis loop when subjected to bipolar periodic excitation.[4] Memristors and memristor-based architectures have recently aroused considerable research interests.[5−10] Memristors can emulate biological synapses, which can be used to build brainlike computers.[5,11,12] Furthermore, memristors have demonstrated both storage and stateful logic operations in the same device.[6] Memristor-based neuromorphic computing and nonvolatile logic have the potential to solve the von Neumann bottleneck problem of conventional digital computers,[13] which may revolutionize computer research in the coming decades.[14]

Resistive random access memory (RRAM) has also recently been linked to the concept of memristor.[15,16] In fact, most memristors that have previously been reported in the literature are generic ones (i.e., memristive systems) rather than ideal ones (i.e., perfect memristor).[3,15,17,18] The resistance of an ideal memristor depends only on the charge or flux that flows through the system, so most memristors reported to date are actually not memristors but memristive systems.[19] The unambiguous flux-charge constitutive relation and the charge-(flux-) controlled state equation are indispensable for describing ideal memristors.[15,18] Furthermore, ideal memristors should exhibit a pinched hysteresis loop, frequency-dependent loop areas, and continuously tunable resistance. However, ideal memristors are probably rare, and a notable exception is a small dissipative component in Josephson junctions.[17] Therefore, fabricating an actual physical ideal memristor is exciting and desirable.

The alkaline-earth-ion-doped perovskite manganite $La_{1-x}Sr_xMnO_3$ ($0.2 < x < 0.5$, LSMO) is a typical colossal

Received: August 20, 2013
Accepted: October 1, 2013
Published: October 1, 2013

  

magnetoresistance (CMR) material.[20] We have very recently demonstrated that amorphous $La_{1-x}Sr_xMnO_3$ (a-LSMO) thin films exhibit excellent nonvolatile bipolar resistive switching properties on the basis of the electrochemical metallization (ECM) hypothesis.[21] Hence, it should be possible to combine memristor and CMR properties in one material, which is especially appealing. However, high-frequency-dependent properties are very crucial for identifying memristors,[19] and most research to date has only shown the quasi-static current−voltage ($I$−$V$) curves or hysteresis curves measured at relatively low frequencies.[7,22,23] Here, we demonstrate a new a-LSMO-thin-film-based analog memristor, which shows high-frequency-dependent pinched hysteresis loops.

## EXPERIMENTAL SECTION

**Sample Preparation.** Radio frequency (RF; 13.56 MHz) magnetron sputtering and a 60 mm diameter sintered stoichiometric $La_{0.7}Sr_{0.3}MnO_3$ ceramic target (>99.9%) were used to deposit a 20 nm thick LSMO thin film onto commercial Pt/Ti/$SiO_2$/Si substrates. The base pressure in the sputter chamber was $<5 \times 10^{-4}$ Pa, and the target was sputtered for 15 min in an atmosphere consisting of 80% argon and 20% oxygen. The temperature of the substrate was 50 °C. The working pressure and RF power were maintained at 0.8 Pa and 50 W. Several 50 $\mu$m diameter, 100 nm thick Ag electrodes were deposited using direct-current magnetron sputtering with a metal shadow mask.

**Measurements.** Field-emission transmission electron microscopy (TEM, FEI Tecnai F20 microscope operated at 200 kV) was used for $Z$-contrast scanning TEM (STEM), high-resolution TEM (HR-TEM), and energy-dispersive X-ray spectroscopy (EDX) mapping analyses. Atomic force microscopy (AFM, NT-MDT Solver) with a PtIr-coated Si tip was used for conductive AFM (C-AFM) analysis, and the scanning speed was set to 1 Hz. The transient $I$−$V$ and quasi-static voltage-(current)-sweep characteristics of the Ag/a-LSMO/Pt memristor were measured using a Keithley 4200 semiconductor characterization system (4200-SCS) with a Cascade Microtech Summit 11000 probe station. The positive bias was defined as the current flowing from the top electrode (TE) to the bottom electrode (BE). We used the KTEI software (V8.2-PC) to control the ultrafast $I$−$V$ module (4225-PMU) and two remote amplifier/switch modules (4225-RPM) on the 4200-SCS, which simultaneously measured the ultrafast current and voltage. Triangular-waveform voltage pulses were generated using the 4200-SCS, and the frequency was calculated from the period of the pulses. The low-temperature resistances were measured using a Lakeshore TTP4 probe station with an Agilent 4155C semiconductor parameter analyzer under vacuum, and liquid nitrogen was used as the refrigerant.

## RESULTS AND DISCUSSION

RF magnetron sputtering was used to deposit the a-LSMO films onto the Pt/Ti/$SiO_2$/Si substrates, and the chemical composition of the films was determined to be $La_{0.79}Sr_{0.21}MnO_3$ with few oxygen vacancies (see Figure S1 in the Supporting Information). We used a-LSMO sandwiched between an Ag TE and a Pt BE to fabricate the memristor device (see Figure S2 in the Supporting Information). The layered structure consisted of Ag (100 nm)/a-LSMO (20 nm)/Pt (150 nm)/Ti (50 nm)/$SiO_2$ (500 nm)/Si. Figure 1a,b shows the cross-sectional $Z$-contrast STEM image generated under high-angle annular dark-field (HAADF) mode and the EDX elemental-mapping images of Pt, Ag, and Mn, which reveal that the Ag/a-LSMO/Pt layered-structure memristor shows clear interfaces. The HR-TEM image of the LSMO film shown in Figure 1c reveals a lack of long-range order, and the diffuse halos of the fast Fourier transformation pattern in the inset of Figure 1c indicate that the LSMO film is amorphous (see Figure S3 in the Supporting Information). The as-fabricated memristors were insulative and

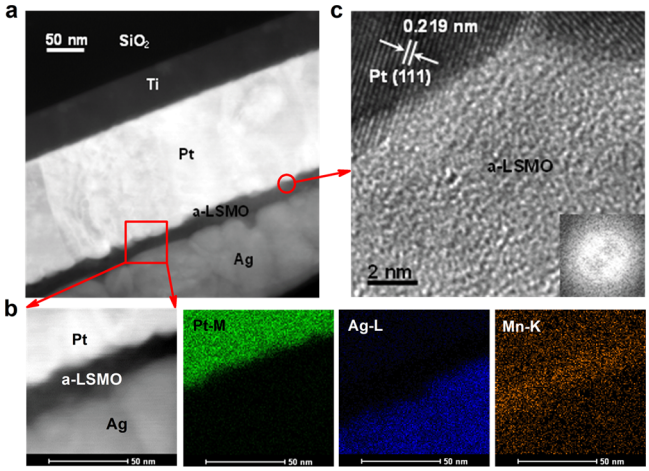


**Figure 1.** (a) Cross-sectional $Z$-contrast HAADF-STEM image of the Ag/a-LSMO/Pt memristor. (b) Enlarged images of the region indicated by the red square in panel a as well as the EDX elemental-mapping images of the Pt, Ag, and Mn. (c) HR-TEM image of the a-LSMO/Pt interface. The inset shows the fast Fourier transformation pattern of the LSMO film.

showed high cell resistance ($\approx 10^8$ Ω) because of the discontinuous −Mn−O−Mn−O− chains in the amorphous Manganite, and the Ag/a-LSMO/Pt memristor must be electroformed to activate it, as shown in Figure 2. A 10 mA current compliance (CC) was used to prevent the dielectric of the memristor from permanently breaking down during electroforming. As shown in Figure 2, the resistance of the cell electroformed using about 0.9 V did not return to the initial value, and the subsequent resistance ratio of the cell was no more than $10^2$.

We now turn our attention toward the dynamic $I$−$V$ characteristics of the memristor, which is the central exploration of this work. We found that the memristor cell electroformed with a 10 mA CC exhibited excellent memristive properties. Figure 3a shows the typical dynamic current response of a 1 V amplitude, 2 $\mu$s period triangular-waveform voltage pulse. The CC was set to 10 mA during the transient test. The analyzer decreased the amount of voltage applied to the cell as soon as the CC was reached, so there was some change in the actual waveform of the programmed triangular pulse, and the peak voltage could not reach 1 V, as shown in Figure 3a. Figure 3b shows a typical $I$−$V$ hysteresis loop corresponding to the dynamic current response shown in Figure 3a. The hysteresis loop is zero-crossing and pinched and is confined to the first and third quadrants of the voltage−current plane, and the excitation frequency is 500 kHz. Figure 3c shows the pinched hysteresis loops measured at 1.25 MHz, 500 kHz, and 500 Hz. As shown in Figure 3c, the area enclosed by the pinched hysteresis loops shrinks with the increasing frequency of the forcing voltage. The pinched hysteresis loops degenerated into almost a straight line as the frequency was increased to 2.5 MHz. On the basis of our test results for different cells (see Figure S4 in the Supporting Information), we can also imagine that the memristor may eventually reduce to a purely linear resistor as the frequency approaches infinity because the memristor shows certain inertia and cannot respond as rapidly as the fast variation in the excitation waveform and must therefore settle into some equilibrium state.[19] The shrinking area enclosed by the pinched hysteresis loops with increasing excitation frequency is a characteristic

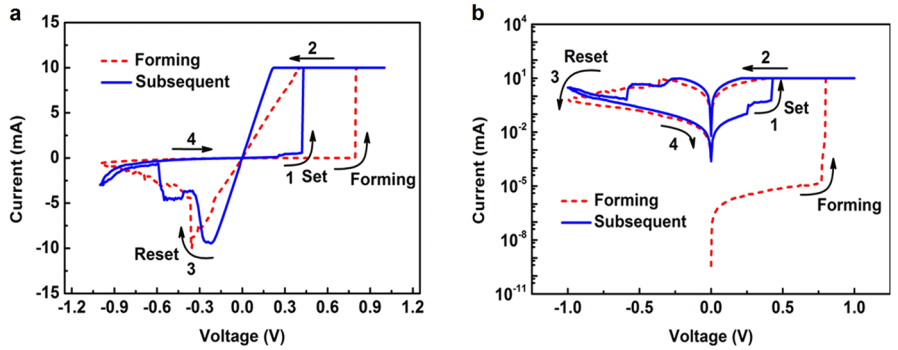


**Figure 2.** Initial electroforming and the typical subsequent quasi-static $I-V$ cycles for the Ag/a-LSMO/Pt memristor cells with a 10 mA CC shown on a (a) linear scale and (b) semilogarithmic scale.

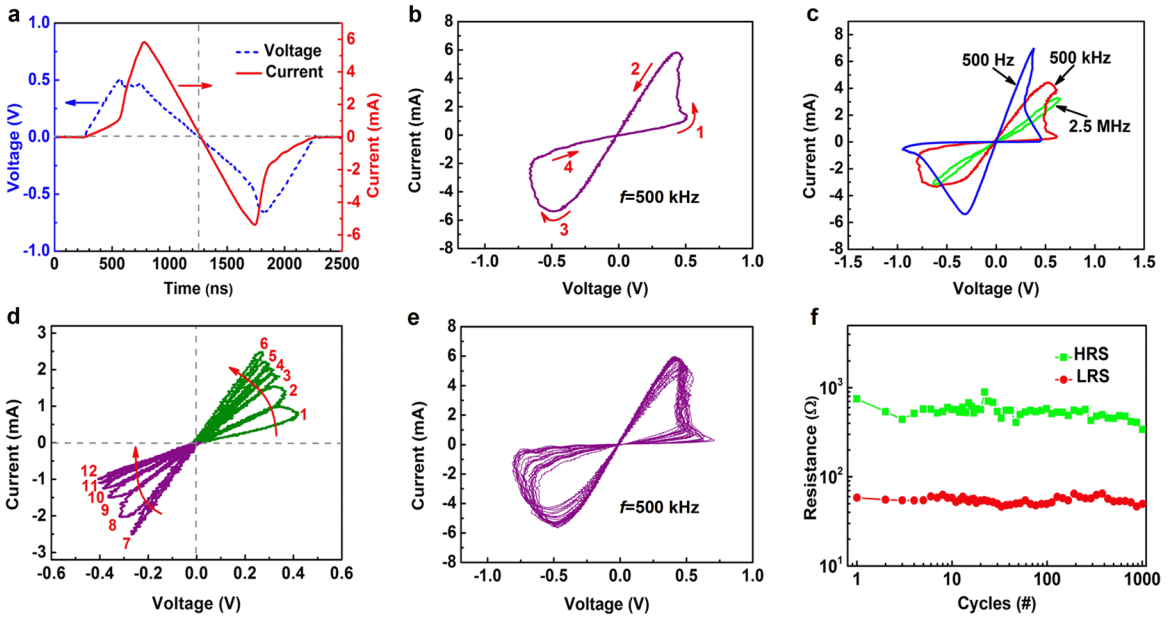


**Figure 3.** (a) Dynamic current response typical of a 1 V amplitude, 2 $\mu$s period, triangular-waveform voltage pulse (0 → 1 V → 0 → −1 V → 0; rise time = 500 ns). The CC was set to 10 mA to protect the memristor from permanently breaking down during the transient test. (b) $I-V$ hysteresis loop for the Ag/a-LSMO/Pt memristor corresponding to the curves in panel a; the excitation frequency is 500 kHz. (c) $I-V$ hysteresis curves for the Ag/a-LSMO/Pt memristor measured at 2.5 MHz, 500 kHz, and 500 Hz. (d) Memristor resistance continuously decreases (or increases) during the positive (or negative) voltage pulses. Numbers 1−12 label successive $I-V$ curves measured under the applied 400 ns period positive/negative triangular-waveform voltage pulses (0 → ± 0.6 V → 0; rise time = 200 ns). (e) Twenty-five sequential $I-V$ hysteresis loops measured at 500 kHz for the Ag/a-LSMO/Pt memristor. (f) Evolution of resistances of HRS and LRS in 1000 consecutive set−reset cycles. The write/read/erase/read sequence is continuously applied using writing (1 V, 1 $\mu$s), erasing (−1.5 V, 5 $\mu$s), and reading (50 mV, 2 $\mu$s) pulses.

typical of memristors and consequently the Ag/a-LSMO/Pt cells that we fabricated were indeed memristors; however, such characteristic has seldom been reported in the literature. Figure 3d shows the continuously tunable resistance of our memristor. Six consecutive positive (and negative) triangular-waveform voltage pulses (0 → ± 0.6 V → 0; period = 400 ns) clearly result in a continuous decrease (or increase) in the resistance of the memristor, and the overall resistance of the memristor was determined by the history of the pulses applied to it. This behavior is analogous to that found in a neurological synapse; thus, our memristor can be considered as an electrical synapse.[24] Furthermore, we measured the endurance performance of the Ag/a-LSMO/Pt memristor. Figure 3e shows 25 sequential $I-V$ hysteresis loops measured at an excitation frequency of 500 kHz, and Figure 3f shows the evolution of the resistances at a high-resistance state (HRS) and a low-resistance state (LRS) for 1000 consecutive set−reset cycles and writing (1 V, 1 $\mu$s), erasing (−1.5 V, 5 $\mu$s), and reading (50 mV, 2 $\mu$s) pulses. The memristive performances clearly show no obvious degradation after 25 repeating-pulse $I-V$ cycles, and the resistance ratio (i.e., the ratio of HRS to LRS) was about 10 and varied insignificantly during the 1000 set−reset pulse tests, indicating that the Ag/a-LSMO/Pt memristors are highly reliable and reproducible (see Figure S5 in the Supporting Information).

C-AFM studies were performed, as schematically shown in Figure 4a, to gain insight into how electroforming affected the microstructure of the memristors. We first measured the local $I-V$ of a single point by sweeping the BE bias. As shown in Figure 4b, the PtIr-coated Si nanotip could also trigger electroforming. The electroforming voltage of about 6 V measured here was higher than that of about 0.9 V, as shown in Figure 2, possibly because of the additional energy barrier and nonuniform electric field caused by the C-AFM nanotip.[25] C-

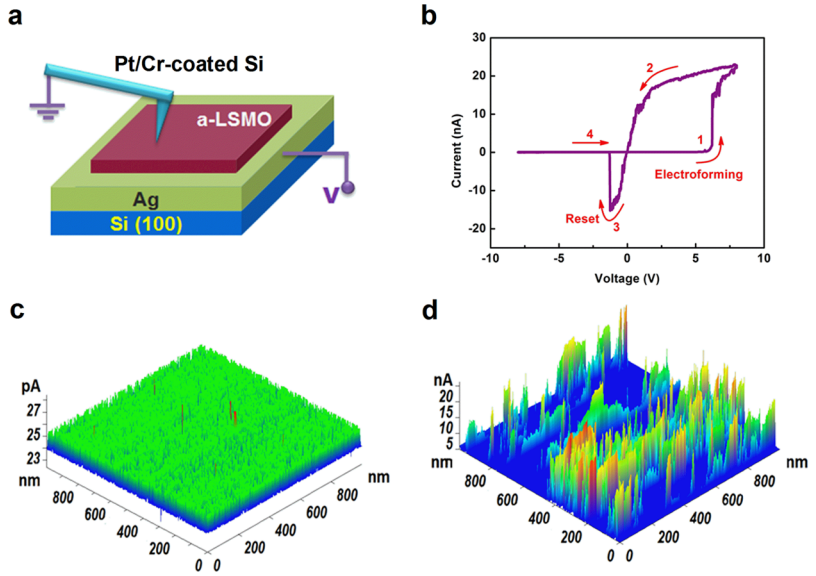


**Figure 4.** Using C-AFM to observe Ag/a-LSMO/Pt memristor electroforming. (a) Schematic of measurement setup and cell structure. (b) Quasi-static *I*−*V* characteristic measured using the C-AFM tip as the TE. Current-mapping images measured at (c) a 1 V reading bias and (d) a 5 V writing bias.

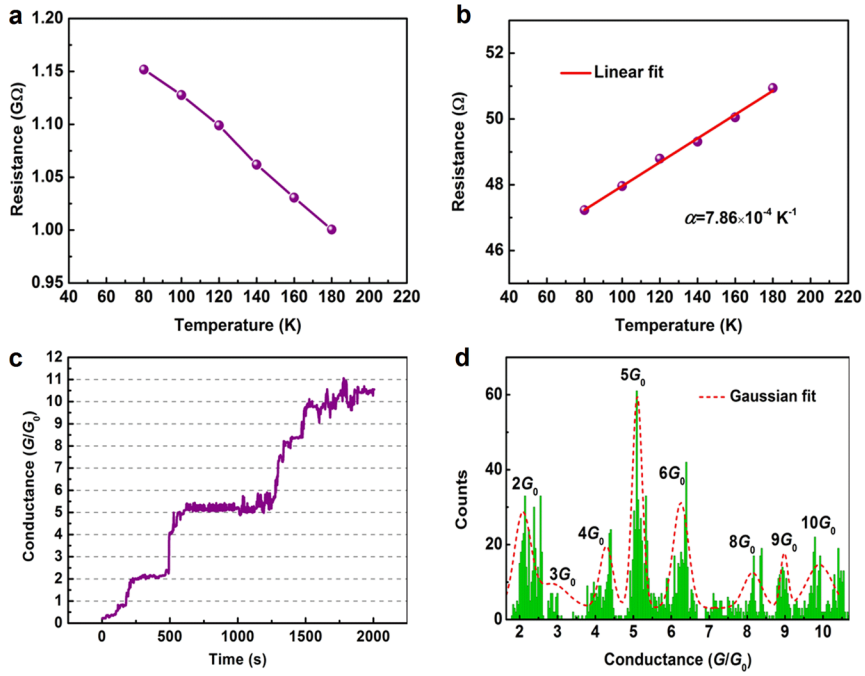


**Figure 5.** Low-temperature dependence of resistances of (a) HRS and (b) LRS of the Ag/a-LSMO/Pt memristor measured during electroforming. (c) Quantized cell conductance analyzed by sweeping the current. The current is increased stepwise from 1 to 100 $\mu$A at 100 nA and 2 s per step. (d) Cumulative statistics for Ag/a-LSMO/Pt memristor conductivity measured at more than 2000 points.

AFM analysis was then performed at a 1 V reading bias for the pristine sample, and the whole scanned area exhibited uniformly low current because the amorphous films show uniform morphology, as shown in Figure 4c. Many conductance peaks, corresponding to localized high-conduction regions, emerged when a 5 V writing bias was applied to the pristine sample, as shown in Figure 4d. The C-AFM current-mapping images provide direct evidence of conduction channels forming as our memristor was being electroformed. We also measured the low-temperature (i.e., 80−180 K) resistances of the HRS and LRS as the memristor was being electroformed with a 10 mA CC. The resistance of the HRS in Figure 5a shows behavior typical of insulators. However, the resistance of the LRS in Figure 5b exhibits electronic transport behavior typical of metals, and the temperature coefficient of resistance $\alpha$ was calculated as $7.6 \times 10^{-4}$ $K^{-1}$, which is close to that for Ag nanowire,[26] by linear fitting the resistance data of the memristor. This result suggests that the conduction channels shown in the C-AFM images in Figure 5 originate from the Ag nanofilaments formed as our memristor was electroforming, which is consistent with the ECM hypothesis.[27]

We found multiple current jumps in discrete steps during electroforming and RS processes under quasi-static voltage (or current) sweep (see Figure S6 in the Supporting Information). We used a current-sweep method to study electroforming in detail.[28] The electrical conductance, $G = I/V$, was recorded in units of quantum conductance, $G_0 = 2e^2/h = 78\ \mu S = 1/(12.9\ k\Omega)$, where $e$ represents the charge of an electron, and $h$ is Planck's constant.[29] Figure 5c clearly shows several abrupt changes in conductance, with each followed by a stable conductance plateau. We found that most of the changes in conductance occurred at integer multiples of $G_0$ (see Figure S7 in the Supporting Information). The conductance state was also evaluated from more than 2000 measurement points in different cells, and the cumulative statistics were calculated, as shown in Figure 5d. Most of the peaks were concentrated around the integer multiples of $G_0$, clearly demonstrating a quantized conductance behavior that should be ascribed to the atomic-scale changes in the dimension of the Ag nanofilaments.[30]

$G_0$, the conductance of a single Ag atom bridge between the BE and TE, is a natural physics-based boundary between the tunneling and nanofilament-bridge states.[31] When $G < G_0$, the memristor is in a tunneling state and a spatial gap exists in the nanofilament; when $G > G_0$, it is in a nanofilament-bridge state, and an Ag nanofilament behaves as a quantum wire, which can be as narrow as a single-atom conduction path or a thicker Ag nanofilament showing classical metallic properties.[32] Importantly, we found that only memristors electroformed under a 10 mA or higher CC easily exhibited high-frequency pinched hysteresis loops. For example, the memristor initially electroformed under a 10 mA CC, as shown in Figure 2, easily exhibited excellent high-frequency pinched hysteresis loops, as shown in Figure 3. We also found that the HRS resistances of subsequent memristive $I-V$ cycles for the memristor electroformed under a 10 mA or higher CC were all below 12.9 kΩ $(1/G_0)$. For example, the HRS resistance of the subsequent cycle shown in Figure 2 is only about 2860 Ω (read at 50 mV); all of the HRS resistances shown in Figure 3e are below 12.9 kΩ, and the average HRS resistance shown in Figure 3f is only about 800 Ω. The HRS resistances below 12.9 kΩ ($G > G_0$) indicate that the memristor is in a nanofilament-bridge state. Thicker Ag nanofilaments form under higher CCs, and such nanofilaments are difficult to dissolve by reversing bias voltages, so the residual Ag nanofilament was still bridging the Ag TE and Pt BE after the memristor had been electroformed. Therefore, the high-frequency pinched hysteresis loops shown in Figure 3 occurred while the memristor was in a nanofilament-bridge state.

The memristor, exhibiting high-frequency pinched hysteresis loops, is in a nanofilament-bridge state, so the memristive resistance (i.e., memristance, $R$) is determined by the diameter of the Ag nanofilament. According to the ECM theory and Faraday's law, the nanofilament diameter ($d$) is determined by the supplied ionic charge, which in turn is determined by the time integral of the ionic current. When a positive voltage is applied to the Ag TE, the anode dissolves because of the electrochemical potential difference; hence, $Ag^+$ cations are generated. The $Ag^+$ cations under the action of the strong electric field then migrate across the solid-electrolyte-like a-LSMO layer toward the Pt BE, where the $Ag^+$ cations are reduced according to the cathodic deposition reaction $Ag^+ + e^- \rightarrow Ag$. More Ag atoms are produced when more ionic current and charges are supplied, resulting in thicker Ag nanofilaments, and vice versa. The total external memristor current is the sum of the electronic and ionic currents. Considering the 1D growth of a cylindrical Ag nanofilament,[27] we can derive the following equation

$$d = \left(\frac{4\beta qM}{\pi e N_A \rho l} + {d_0}^2\right)^{1/2} \quad (1)$$

where $\beta$ represents the percentage of charge supplied by the ionic current, $q$ represents the total amount of charge supplied by the external current, $M$ represents the molar mass of Ag, $e$ represents the charge of an electron, $N_A$ is the Avogadro constant, $\rho$ represents the density of Ag, and $d_0$ represents the initial diameter of the electroformed Ag nanofilament. In view of the thickness of the a-LSMO, the length ($l$) of the filament connecting the TE and BE is about 20 nm, which is comparable to the mean free path ($l_{mfp}$) of Ag nanowire.[26] When $d$ is comparable to the electron Fermi wavelength $\lambda_F$ (about 0.5 nm for Ag[33]), the transport in Ag nanofilaments falls into the ballistic regime, which is described by the Landauer formula. As shown in Figure 5c, the nanofilaments exhibit discrete resistances, given by $R = 1/[G_0 \mathrm{Int}(2d/\lambda_F)T]$, where $\mathrm{Int}(x)$ represents the integer just smaller than $x$ and $T$ represents the transmission probability, showing a stepwise variation with $d$.[34] When more ionic current and charges are supplied, $d$ becomes larger. When $d$ is larger than $\lambda_F$ but still comparable to or smaller than $l_{mfp}$, as shown in Figure 4d, the transport in Ag nanofilaments falls into the classical finite size regime where the scattering events at the nanofilament surface or grain boundary alter the transport behavior. Here, the resistivity ($r$) of the Ag nanofilaments becomes larger than that of bulk on the basis of the Fuchs−Sondheimer and Mayadas−Shatzkes models[35] and is related with $d$ because of the size and surface effects, given by $R = 4r(d)l/(\pi d^2)$, where $r(d)$ is a function of $d$.

In view of these considerations, $R$ is therefore a function of $d$, which is determined by $q$, as shown in eq 1, so $R$ is also therefore the function of $q$. Consequently, we can derive the following equations

$$V(t) = R(q)I(t) \quad (2)$$

$$dq/dt = I \quad (3)$$

where $V(t)$ represents the voltage, $I(t)$ represents the current, and $t$ represents time. Here, $q$ acts as a state variable, and $R$ represents a nonlinear resistance depending on $q$ that varies over time, as described in eq 3. Equations 2 and 3 demonstrate that the Ag/a-LSMO/Pt device behaves like an analog memristor.[3,15] Ultimately, the frequency-dependent pinched hysteresis loops originate from the change in the quantities of charge across the memristor. More charges are injected into/out of the memristor at low frequencies, so the change in the amplitude of the nanofilament diameter (i.e., resistance) is larger, and the area enclosed by the corresponding hysteresis loop is larger. The diameter (i.e., resistance), however, changes insignificantly at very high frequencies because of few charges across the memristor, so the area enclosed by the corresponding hysteresis loop becomes smaller. The memristor is in a nanofilament-bridge state when the hysteresis loops are pinched. Furthermore, many nanovoids or open channels exist in the long-range-disorder sputtered a-LSMO thin films, and the nanovoids and open channels are large enough to gradually increase the diameter of the Ag nanofilament. When the frequency reaches 500 Hz (see Supporting Information in the

Figure S4), the area enclosed by the pinched hysteresis loop does not further increase with decreasing frequency because the limited space of nanovoids and open channels in the a-LSMO prevent the diameter of the nanofilament from further increasing. Therefore, this memristor is based on Ag nanofilaments thickening/thinning in a-LSMO thin films, which is different from nanofilaments forming/rupturing in conventional RRAM cells.[36]

Oxygen vacancies can diffuse in metal oxides.[37] The memristive performances should be independent of the TE materials if oxygen vacancies play some role in the Ag/a-LSMO/Pt analog memristor. However, we found that only the devices fabricated using electrochemically active metals such as Ag or Cu as TE materials could exhibit memristive properties (see Figure S8 in the Supporting Information). Therefore, memristive properties because of the oxygen vacancies in a-LSMO can be ruled out. The a-LSMO thin films in this memristor show high ion conduction under strong electric fields and act as a solid electrolyte for $Ag^+$ cations.[38] However, a-LSMO films are not conventionally viewed as solid electrolytes for $Ag^+$ cations such as those in $Ag_2S$.[39] A wide variety of nanovoids and open channels may exist in sputtered a-LSMO thin films because of the long-range-disorder structure, which are natural pathways for $Ag^+$ cation transport. Furthermore, the prepared a-LSMO films are very thin (≈20 nm), meaning that applying modest applied voltages to the memristor can produce strong electric fields, enabling $Ag^+$ cations to travel easily across the film and form an Ag nanofilament.[21] Thus, a-LSMO thin films can act as solid electrolytes, exhibiting high ion mobility and fast response time.

## CONCLUSIONS

We used a-LSMO thin films to develop an analog memristor. The Ag/a-LSMO/Pt memristor notably exhibited excellent pinched hysteresis loops under high excitation frequency, and the area enclosed by the pinched hysteresis loops shrank with increasing excitation frequency. The memristor also showed continuously tunable synapselike resistance and stable endurance (up to 1000 set−reset pulse cycles). The C-AFM current-mapping images and the low-temperature-dependent resistances of the HRS and LRS showed that Ag nanofilaments had formed during electroforming. The a-LSMO thin films in this memristor acted as a solid electrolyte for $Ag^+$ cations, and only the Ag/a-LSMO/Pt cells electroformed to an HRS resistance below $1/G_0$ easily exhibited high-frequency pinched hysteresis loops. On the basis of the ECM theory and electrical transport models of quantum wires and nanowires, we derived that the memristance, $R$, was ultimately determined by the amount of charge, $q$, supplied by the external current. The state equations for the memristor were established, and $q$ was the state variable. This study provided a new analog memristor based on metal nanofilaments thickening/thinning in ECM cells, which could be extended to other RRAM materials. This memristor may enable the development of beyond von Neumann computers.

## ASSOCIATED CONTENT

### Supporting Information

Composition and morphology of the a-LSMO thin films, photograph of the Ag/a-LSMO/Pt memristor device, pinched hysteresis loops measured at various frequencies, $I-V$ curves showing conductance quantization, and $I-V$ curves for the a-LSMO-based memristor structure fabricated using various TE materials. This material is available free of charge via the Internet at http://pubs.acs.org.

## AUTHOR INFORMATION

### Corresponding Author

*E-mail: hfcheng@rocketmail.com.

### Notes

The authors declare no competing financial interest.

## ACKNOWLEDGMENTS

We thank Drs. Xun Yi, Jingyue Fang, and Ming Wang for fruitful discussions. We also thank Yulei Hu and Zongpeng Zhu for helpful experimental assistance. This work was supported by the Aid Program for Innovative Group of National University of Defense Technology and the National Natural Science Foundation of China (21203248).

## REFERENCES

(1) Chua, L. *IEEE Trans. Circuit Theory* **1971**, *18*, 507−519.
(2) Prodromakis, T.; Toumazou, C.; Chua, L. *Nat. Mater.* **2012**, *11*, 478−481.
(3) Strukov, D. B.; Snider, G. S.; Stewart, D. R.; Williams, R. S. *Nature* **2008**, *453*, 80−83.
(4) Yang, J. J.; Strukov, D. B.; Stewart, D. R. *Nat. Nanotechnol.* **2013**, *8*, 13−24.
(5) Jo, S. H.; Chang, T.; Ebong, I.; Bhadviya, B. B.; Mazumder, P.; Lu, W. *Nano Lett.* **2010**, *10*, 1297−1301.
(6) Borghetti, J.; Snider, G. S.; Kuekes, P. J.; Yang, J. J.; Stewart, D. R.; Williams, R. S. *Nature* **2010**, *464*, 873−876.
(7) Chanthbouala, A.; Garcia, V.; Cherifi, R. O.; Bouzehouane, K.; Fusil, S.; Moya, X.; Xavier, S.; Yamada, H.; Deranlot, C.; Mathur, N. D.; Bibes, M.; Barthélémy, A.; Grollier, J. *Nat. Mater.* **2012**, *11*, 860−864.
(8) Younis, A.; Chu, D.; Lin, X.; Yi, J.; Dang, F.; Li, S. *ACS Appl. Mater. Interfaces* **2013**, *5*, 2249−2254.
(9) Huang, C. H.; Huang, J. S.; Lai, C. C.; Huang, H. W.; Lin, S. J.; Chueh, Y. L. *ACS Appl. Mater. Interfaces* **2013**, *5*, 6017−6023.
(10) Berzina, T.; Erokhina, S.; Camorani, P.; Konovalov, O.; Erokhin, V.; Fontana, M. P. *ACS Appl. Mater. Interfaces* **2009**, *1*, 2115−2118.
(11) Wang, Z. Q.; Xu, H. Y.; Li, X. H.; Yu, H.; Liu, Y. C.; Zhu, X. J. *Adv. Funct. Mater.* **2012**, *22*, 2759−2765.
(12) Kim, H.; Sah, M. P.; Yang, C.; Roska, T.; Chua, L. O. *Proc. IEEE* **2012**, *100*, 2061−2070.
(13) Hasegawa, T.; Terabe, K.; Tsuruoka, T.; Aono, M. *Adv. Mater.* **2012**, *24*, 252−267.
(14) Kozma, R.; Pino, R. E.; Pazienza, G. E. *Advances in Neuromorphic Memristor Science and Applications*; Springer: New York, 2012; p 9.
(15) Chua, L. *Appl. Phys. A: Mater. Sci. Process.* **2011**, *102*, 765−783.
(16) Valov, I.; Linn, E.; Tappertzhofen, S.; Schmelzer, S.; van den Hurk, J.; Lentz, F.; Waser, R. *Nat. Commun.* **2013**, *4*, 1771.
(17) Pershin, Y. V.; Ventra, M. D. *Adv. Phys.* **2011**, *60*, 145−227.
(18) Biolek, Z.; Biolek, D.; Biolkova, V. *IEEE Trans. Circuits Syst., II* **2012**, *59*, 607−611.
(19) Chua, L. O.; Sung Mo, K. *Proc. IEEE* **1976**, *64*, 209−223.
(20) Gorkov, L. P.; Kresin, V. Z. *Phys. Rep.* **2004**, *400*, 149−208.
(21) Liu, D. Q.; Wang, N. N.; Wang, G.; Shao, Z. Z.; Zhu, X.; Zhang, C. Y.; Cheng, H. F. *Appl. Phys. Lett.* **2013**, *102*, 134105-1−134105-5.
(22) Song, J.; Zhang, Y.; Xu, C.; Wu, W.; Wang, Z. L. *Nano Lett.* **2011**, *11*, 2829−2834.
(23) Tsurumaki, A.; Yamada, H.; Sawa, A. *Adv. Funct. Mater.* **2012**, *22*, 1040−1047.
(24) Li, Y.; Zhong, Y.; Xu, L.; Zhang, J.; Xu, X.; Sun, H.; Miao, X. *Sci. Rep.* **2013**, *3*, 1619.
(25) Lee, C.; Kim, I.; Choi, W.; Shin, H.; Cho, J. *Langmuir* **2009**, *25*, 4274−4278.

(26) Bid, A.; Bora, A.; Raychaudhuri, A. *Phys. Rev. B* **2006**, *74*, 035426-1−035426-8.
(27) Waser, R.; Dittmann, R.; Staikov, G.; Szot, K. *Adv. Mater.* **2009**, *21*, 2632−2663.
(28) Tappertzhofen, S.; Valov, I.; Waser, R. *Nanotechnology* **2012**, *23*, 145703.
(29) Zhu, X.; Su, W.; Liu, Y.; Hu, B.; Pan, L.; Lu, W.; Zhang, J.; Li, R.-W. *Adv. Mater.* **2012**, *24*, 3941−3946.
(30) Krans, J. M.; van Ruitenbeek, J. M.; Fisun, V. V.; Yanson, I. K.; de Jongh, L. J. *Nature* **1995**, *375*, 767−769.
(31) Zhirnov, V. V.; Meade, R.; Cavin, R. K.; Sandhu, G. *Nanotechnology* **2011**, *22*, 254027.
(32) Long, S.; Lian, X.; Cagli, C.; Cartoixa, X.; Rurali, R.; Miranda, E.; Jiménez, D.; Perniola, L.; Liu, M.; Suñé, J. *Appl. Phys. Lett.* **2013**, *102*, 183505-1−183505-4.
(33) Costa-Kramer, J. L.; Garcia, N.; Olin, H. *Phys. Rev. Lett.* **1997**, *78*, 4990−4993.
(34) Datta, S. *Electronic Transport in Mesoscopic Systems*; Cambridge University Press: Cambridge, 1995; p 54.
(35) Steinhogl, W.; Schindler, G.; Steinlesberger, G.; Engelhardt, M. *Phys. Rev. B* **2002**, *66*, 075414-1−075414-4.
(36) Wang, Z.; Zeng, F.; Yang, J.; Chen, C.; Pan, F. *ACS Appl. Mater. Interfaces* **2012**, *4*, 447−453.
(37) He, L.; Liao, Z.-M.; Wu, H.-C.; Tian, X.-X.; Xu, D.-S.; Cross, G. L. W.; Duesberg, G. S.; Shvets, I. V.; Yu, D.-P. *Nano Lett.* **2011**, *11*, 4601−4606.
(38) Valov, I.; Sapezanskaia, I.; Nayak, A.; Tsuruoka, T.; Bredow, T.; Hasegawa, T.; Staikov, G.; Aono, M.; Waser, R. *Nat. Mater.* **2012**, *11*, 530−535.
(39) Liao, Z.-M.; Hou, C.; Zhao, Q.; Wang, D.-S.; Li, Y.-D.; Yu, D.-P. *Small* **2009**, *5*, 2377−2381.